Check for updates

ADVANCED ENERGY MATERIALS
www.advenergymat.de

Regulating the Water Dissociation on Atomic Iron Sites to Speed Up CO_2 Protonation and Achieve pH-Universal CO_2 Electroreduction

Qi Tang, Qi Hao, Junxiu Wu, Yaowen Zhang, Ping Sun, Depeng Wang, Chuan Tian, Haixia Zhong, Yihan Zhu, Keke Huang, Kai Liu,* Xinbo Zhang,* and Jun Lu**

Atomic Fe sites enabled electrochemical carbon dioxide (CO_2) reduction (ECO_2R) to carbon monoxide (CO) at low overpotentials. However, the narrow potential ranges for selective CO_2 conversion on atomic Fe sites hindered the CO production at high current densities. Therefore, unveiling the CO_2 electroreduction processes and clarifying the catalytic mechanisms on different atomic Fe sites are important for better design of atomic Fe catalysts toward efficient ECO_2R. Herein, the ECO_2R processes on single-atom, dual-atom, and cluster Fe sites are systematically investigated, and clarify that the balanced water dissociation and CO_2 protonation on dual-atom Fe sites promote the efficient CO production. The dual-atom Fe catalyst achieves Faradaic efficiencies of CO (FE_{CO}) above 92% over a wide potential range of −0.4–−0.9 V versus reversible hydrogen electrode and maintains FE_{CO} of 91% after 153-h electrolysis in H-type cell. Benefitting from the favorable CO_2 protonation for ECO_2R on dual-atom Fe sites, pH-universal CO_2 electroreduction is achieved in alkali-/acid-/bicarbonate-fed membrane electrode assembly electrolyzer, with FE_{CO} exceeds 98% in strongly acidic/alkaline and neutral mediums. The work reveals a water dissociation-promoted CO_2 electroreduction on dual-atom Fe sites and presents a feasible regulation of atomic Fe sites for highly active/selective ECO_2R.

1. Introduction

Electrochemical carbon dioxide (CO_2) reduction (ECO_2R) to value-added chemicals/fuels provides a practicable way for realizing the recycle of emitted CO_2 and alleviating the greenhouse effect.[1] Among electrochemical CO_2 conversions, ECO_2R to carbon monoxide (CO) demonstrates the greatest potential for industrialized CO_2 electrolysis, due to the high activity and selectivity in ECO_2R-to-CO (Faradaic efficiency (FE) >95%, partial current densities ≥200 mA cm^{-2}) and the low cost for CO production/separation (minimum cost for ECO_2R to CO: \$0.13 kg^{-1}; separation cost for CO product via pressure swing adsorption technology: \$10 t^{-1}).[2] The CO product from ECO_2R could be processed via electrochemical CO reduction reaction and Fischer–Tropsch process for synthesizing long-chain organic chemicals.[1–3] Therefore, ECO_2R to CO provides a sustainable transit route to achieve efficient utilization of CO_2.

Q. Tang, D. Wang, H. Zhong, X. Zhang
Changchun Institute of Applied Chemistry
Chinese Academy of Sciences
Changchun, Jilin 130022, China
E-mail: xbzhang@ciac.ac.cn

Q. Tang, D. Wang, H. Zhong, X. Zhang
School of Applied Chemistry and Engineering
University of Science and Technology of China
Hefei, Anhui 230026, China

Q. Hao, K. Liu
School of Engineering
Westlake University
Hangzhou, Zhejiang 310030, China
E-mail: liukai@westlake.edu.cn

The ORCID identification number(s) for the author(s) of this article can be found under https://doi.org/10.1002/aenm.202401364

DOI: 10.1002/aenm.202401364

J. Wu, J. Lu
College of Chemical and Biological Engineering
Zhejiang University
Hangzhou, Zhejiang 310027, China
E-mail: junzoelu@zju.edu.cn

Y. Zhang, K. Huang
State Key Laboratory of Inorganic Synthesis and Preparative Chemistry
College of Chemistry
Jilin University
Changchun, Jilin 130012, China
E-mail: kkhuang@jlu.edu.cn

P. Sun, Y. Zhu
Center for Electron Microscopy
State Key Laboratory Breeding Base of Green Chemistry Synthesis Technology and College of Chemical Engineering
Zhejiang University of Technology
Hangzhou, Zhejiang 310014, China

 © 2024 Wiley-VCH GmbH

To achieve highly active and selective electrochemical conversion of CO_2 to CO, transition metal single-atom catalysts (SACs) have been developed (e.g., Mn,[4] Fe,[5] Co,[6] Ni,[7] Cu,[8] Zn,[9] Ca,[10] Mg[11] SACs) and achieved near 100% selectivity toward CO product in ECO_2R. Among the various SACs, Fe-nitrogen (N)-carbon (C) SACs have attracted widespread attention in potential industrial applications, due to their significantly low overpotentials for driving the CO_2-to-CO reaction.[12] However, the narrow potential ranges of Fe-N-C SACs in selective CO_2 conversion to CO become bottlenecks for delivering CO partial current densities at hundreds of milliampere level.[5,6,13]

More rectently, atomically dispersed Fe catalysts with multi-atom Fe centers exhibit optimized ECO_2R activity/selectivity compared to Fe SACs, allowing them to be considered as promising alternatives.[14] In order to gain more insights into the structural sensitivity toward CO_2 electroreduction to CO from Fe single atoms to dual atoms and clusters, we developed a facile strategy for controllable synthesis of Fe single-atom/dual-atom and cluster catalysts via pyrolysis temperature control from 900 to 1100 °C (named as FeNC-900, FeNC-1000, and FeNC-1100). The coordination environments of Fe species were regulated to FeN_4, Fe_2N_6, and Fe-cluster, respectively. In the evaluation of ECO_2R performance, FeNC-1000 with dual-atom Fe sites achieved FEs of CO (FE_{CO}) above 92% over a wide potential range of −0.4–−0.9 V versus reversible hydrogen electrode (vs RHE), which broke the selectivity limitation of single-atom Fe sites for ECO_2R to CO (maximized FE_{CO} of 66.5% at −0.4 V vs RHE). Then we used in situ attenuated total reflectance-surface-enhanced infrared absorption spectroscopy (ATR-SEIRAS) measurement to monitor the reaction process on different atomic Fe sites. We found that the reaction kinetics of CO_2-to-CO were dependent on the related water dissociation and CO_2 protonation processes. The kinetic equilibrium between proton-feeding from water dissociation and *COOH formation from CO_2 protonation contributed to the promoted CO production. Moreover, the balanced water dissociation and CO_2 protonation also suppressed the competing hydrogen evolution reaction (HER). Benefitting from the favorable CO_2 protonation on dual-atom Fe sites, FeNC-1000 exhibited an excellent stability for CO production, maintaining FE_{CO} of 91% after 153-h continuous electrolysis (−0.5 V vs RHE) in H-type cell. More importantly, FeNC-1000 achieved pH-universal CO_2 electroreduction in alkali-/acid-/bicarbonate-fed membrane electrode assembly (MEA) electrolyzer, with FE_{CO} exceeded 98% in strongly acidic (pH 2)/alkaline (pH 13) and neutral (pH 7) mediums. In the long-term CO_2 conversion to CO at the current density of 100 mA cm^{-2}, FeNC-1000 maintained FE_{CO} of ≈93% after 40-h electrolysis in neutral medium and FE_{CO} of above 97% in a 30-h continuous electrolysis in strongly alkaline electrolyte. Moreover, in strongly acidic medium, FeNC-1000 still maintained the FE_{CO} of ≈90% after a 9-h constant operation. Density functional theory (DFT) calculations indicated that the Fe-Fe bonding in dual-atom Fe sites induced the formation of electron-rich centers, which accelerated CO production and desorption.

Our work revealed the importance of water dissociation on atomic Fe sites for selective CO_2 electroreduction to CO, and clarified that the favorable feeding of protons from water dissociation for CO_2 protonation can accelerate the CO production on dual-atom Fe sites. These findings provided guidance for modulating the coordination environments of atomic Fe sites to improve the catalytic activity and break the selectivity limitation toward CO production.

2. Results and Discussion

The schematic for demonstrating the controllable synthesis of single-atom/dual-atom/cluster Fe catalysts (named as FeNC-900/1000/1100) was displayed in **Figure 1a**. The Fe ions were in situ encapsulated in the polyacrylamide (PAM) gel during the polymerization of acrylamide monomers, which endowed Fe species with a uniform dispersion in the network of PAM gel after freeze-drying. As a templating agent, potassium oxalate was used to induce the formation of porous carbon carriers at high temperatures. Besides, cyanuric acid was selected as N source for facilitating the construction of atomic Fe sites with Fe-N coordination. By modulating the pyrolysis temperatures from 900 to 1100 °C, single-atom/dual-atom/cluster Fe catalysts were obtained, respectively. Figure 1b showed the X-ray diffraction (XRD) patterns of FeNC-900/1000/1100 and metal-free N-doped carbon (NC-1000). Only two broad peaks belonging to graphite (24.1° and 44.1°) were observed, indicating the absence of Fe nanoparticles in FeNC-900/1000/1100.[15] Transmission electron microscopes (TEM) images and the annular patterns in selected area electron diffractions (SAEDs) excluded the presence of aggregated species in FeNC-900/1000 (Figures S1–S3, Supporting Information).[16] Some Fe clusters with an average size of ≈2 nm were observed in the high-resolution TEM graphs of FeNC-1100 (Figure S4, Supporting Information). The N_2 adsorption/desorption isotherms in Figure 1c and Figure S5 (Supporting Information) suggested that the introduction of Fe species increased the specific surface area of carbon supports (Table S1, Supporting Information), which favored the exposure of active sites.[17] In addition, the Raman spectra in Figure 1d showed a higher I_D/I_G ratio (D: disorder band; G: graphite band) of FeNC-1000 compared to that of NC, indicating that the thermal migration of Fe species at high temperatures contributed to the formation of more carbon defects, leading to the favorable anchoring of Fe atoms.[18] To reveal the atomic dispersion of Fe species in different Fe samples, we performed the aberration-corrected high-angle annular dark-field scanning transmission electron microscopy (HAADF-STEM) measurements.[19] As shown in Figure 1e and Figure S6a,b (Supporting Information), no bright aggregates attributed to particle species were found, confirming the atomic-level dispersion of Fe species in FeNC-1000. In Figure 1f,g and Figure S6c (Supporting Information), paired bright dots represented Fe dual atoms were observed in uniform dispersion on the carbon carrier, with an average atom distance of ≈0.23 nm (Figure 1g). The corresponding energy dispersive X-ray spectroscopy (EDS) mappings of FeNC-1000 showed uniform distributions of Fe, C

C. Tian
Jilin Normal University
Key Laboratory of Preparation and Applications of Environmental Friendly Materials
Ministry of Education
Changchun, Jilin 130103, China

© 2024 Wiley-VCH GmbH

16146840, 2024, 40, Downloaded from https://onlinelibrary.wiley.com/doi/10.1002/aenm.202401364 by Changchun Institution Of, Wiley Online Library on [13/01/2025]. See the Terms and Conditions (https://onlinelibrary.wiley.com/terms-and-conditions) on Wiley Online Library for rules of use; OA articles are governed by the applicable Creative Commons License

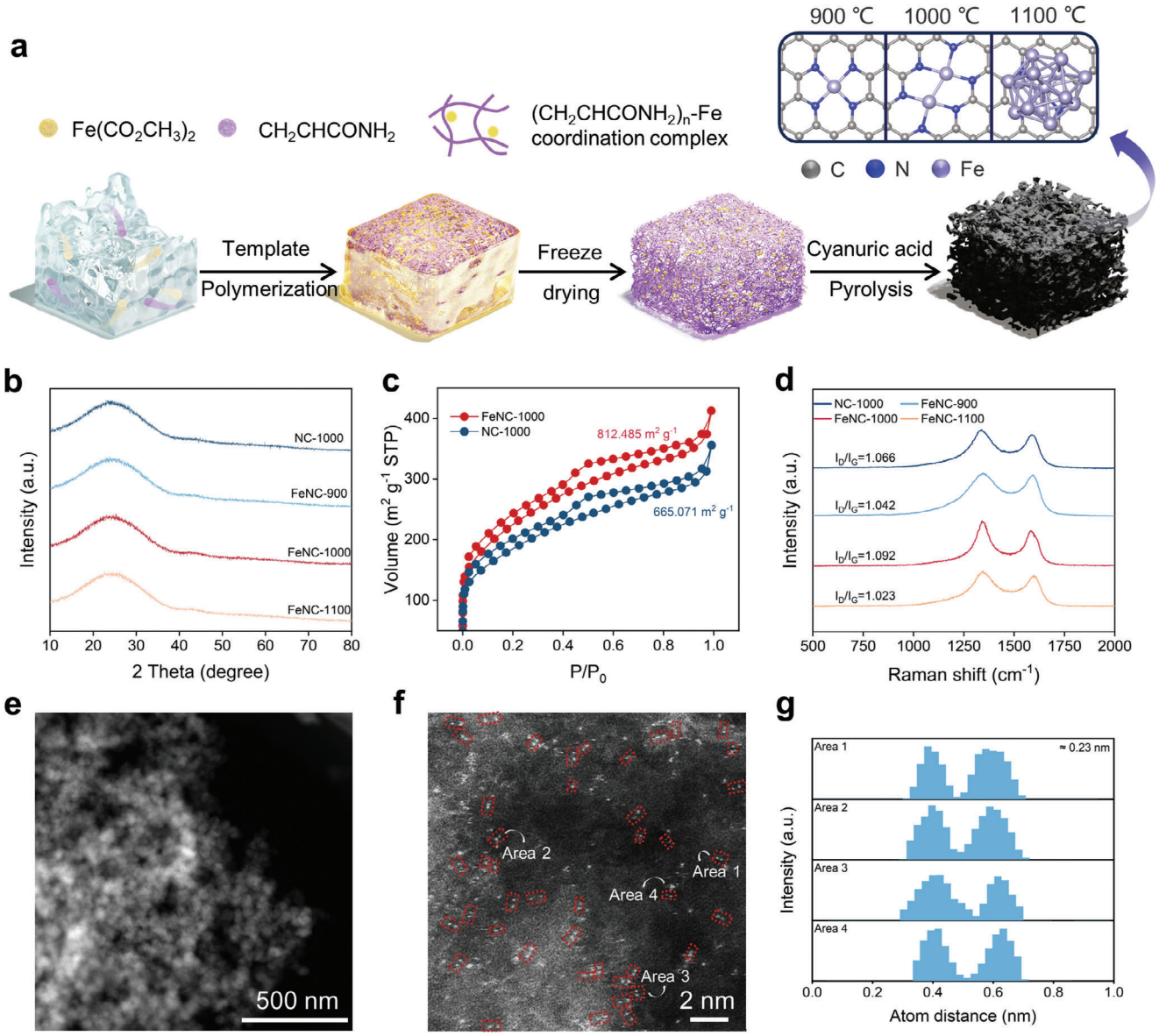

Figure 1. Synthesis concept and structure characterizations. a) Scheme diagram for the synthesis of single-atom/dual-atom/cluster Fe catalysts. b) XRD patterns of NC-1000, FeNC-900, FeNC-1000, and FeNC-1100. c) N_2 adsorption/desorption isotherms of NC-1000 and FeNC-1000. d) Raman spectra of NC-1000, FeNC-900, FeNC-1000 and FeNC-1100. e) Low-resolution HAADF-STEM image of FeNC-1000. f) High-resolution HAADF-STEM image of FeNC-1000. g) The atomic distance of dual atoms in FeNC-1000 based on high-resolution HAADF-STEM in Figure 1f.

and N elements (Figure S6d–g, Supporting Information), which represented the high dispersion of Fe dual atoms.[20] We also demonstrated that the Fe species existed as single atoms and sub-nanometer clusters in FeNC-900 and FeNC-1100, respectively (Figures S7–S9, Supporting Information). Notably, a small number of single/dual atoms were observed in FeNC-1100, suggesting that the formed cluster species originated from the thermal migration/aggregation of Fe atoms at a high temperature (Figure S9, Supporting Information). Therefore, based on the detailed characterizations, we considered that the temperature-dependent evolution of atomic Fe sites originated from the thermal migration of Fe atoms. At 900 °C pyrolysis, Fe species preferred to anchor on the single carbon vacancies containing pyridinic-N sites. When the pyrolysis temperature increased to 1000 °C, the thermally migrated Fe atoms dimerized, forming diatomic Fe sites on the double carbon vacancies. During pyrolysis at 1100 °C, the increased graphitization caused loss of pyridinic-N coordinated carbon vacancies that can anchor Fe atoms, the aggregation effect of Fe atoms induced the formation of atomic Fe clusters. Inductively coupled plasma optical emission spectroscopy (ICP-OES) measurements identified that the Fe loadings in FeNC-900/1000/1100 were 0.84, 0.81 and 0.65 wt%, respectively (Table S2, Supporting Information).

The X-ray photoelectron spectroscopy (XPS) and X-ray adsorption fine structures (XAFS) were conducted to investigate the chemical states and coordination environments of the atomic

© 2024 Wiley-VCH GmbH

16146840, 2024, 40, Downloaded from https://onlinelibrary.wiley.com/doi/10.1002/aenm.202401364 by Changchun Institution Of, Wiley Online Library on [13/01/2025]. See the Terms and Conditions (https://onlinelibrary.wiley.com/terms-and-conditions) on Wiley Online Library for rules of use; OA articles are governed by the applicable Creative Commons License

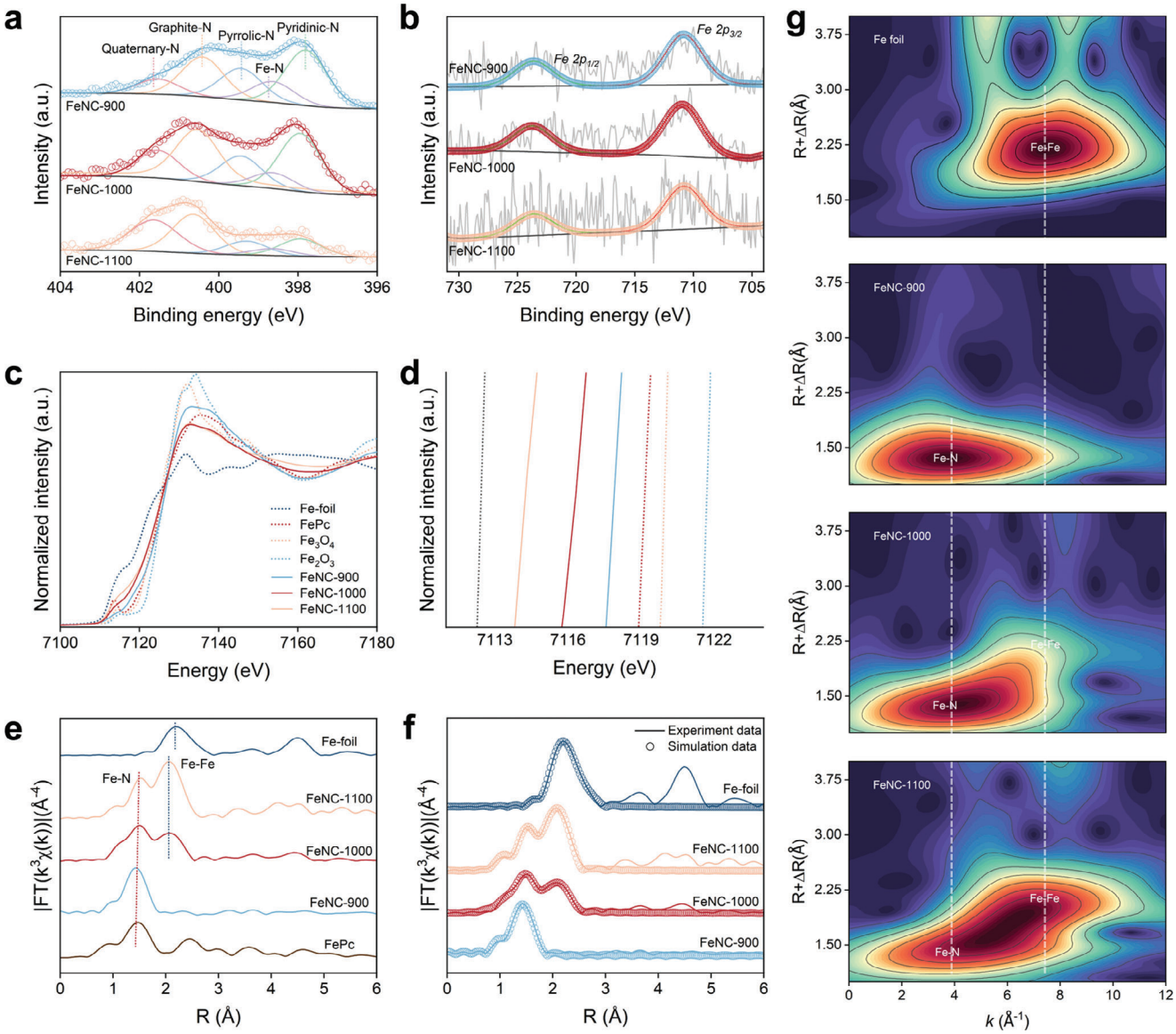

Figure 2. Electronic structure and coordination environment. a) High-resolution N *1s* XPS spectra of FeNC-900, FeNC-1000 and FeNC-1100. b) High-resolution Fe *2p* XPS spectra of FeNC-900, FeNC-1000, and FeNC-1100. c) XANES spectra of Fe foil, FePc, Fe_3O_4, Fe_2O_3, FeNC-900, FeNC-1000, and FeNC-1100 at Fe K-edge. d) Partial enlargement of the adsorption edges in Figure 2c. e) EXAFS spectra of Fe foil, FePc, FeNC-900, FeNC-1000, and FeNC-1100 at Fe K-edge. f) Experimental and fitted EXAFS spectra of Fe foil, FeNC-900, FeNC-1000, and FeNC-1100 at Fe K-edge. G) Wavelet transforms of Fe foil, FeNC-900, FeNC-1000, and FeNC-1100 at Fe K-edge.

Fe sites. In the high-resolution C *1s* XPS spectra (Figure S10, Supporting Information), peaks attributed to C═O, C—O/C—N, C—C/C═C, and satellite peaks of C *1s* were presented in all samples. The N *1s* XPS spectra in **Figure 2a** presents five kinds of N species included pyridine N (398.0 eV), pyrrolic N (399.5 eV), graphite N (400.6 eV), quaternary N (401.6 eV), and Fe—N (398.7 eV). It was noteworthy that the peak area of Fe—N bonding reduced from FeNC-900 to FeNC-1100, suggesting an increase in the proportion of Fe species in metallic state during the evolution from single atoms to clusters.[13a,21] Moreover, Fe—N bonding was not observed in NC (Figure S11, Supporting Information). The high-resolution Fe *2p* spectra showed various binding energies of Fe $2p_{3/2}$ in FeNC-900/1000/1100, which suggests that the Fe—Fe bonding in atomic Fe sites changed the chemical states of Fe species (Figure 2b). The valence states and coordination structures of Fe species were further specified by X-ray near edge fine structures (XANES) and extended X-ray absorption fine structures (EXAFS, Figure S12, Supporting Information). The adsorption edges of FeNC-900/1000/1100 were located between those of Fe foil and iron phthalocyanine (FePc), indicating that the valence states of Fe species in FeNC-900/1000/1100 were between 0 and +2 (Figure 2c,d).[22] The coordination environments of Fe species were clarified from the radial distribution function curves in EXAFS spectra (Figure 2e,f). For Fe foil, the peak at ≈2.19 Å represented the Fe—Fe bonding in the first shell. Two peaks at ≈1.47 and 2.45 Å for FePc were attributed

 © 2024 Wiley-VCH GmbH

16146840, 2024, 40, Downloaded from https://onlinelibrary.wiley.com/doi/10.1002/aenm.202401364 by Changchun Institution Of, Wiley Online Library on [13/01/2025]. See the Terms and Conditions (https://onlinelibrary.wiley.com/terms-and-conditions) on Wiley Online Library for rules of use; OA articles are governed by the applicable Creative Commons License

to Fe—N bonding in the first shell and Fe—C bonding in the second shell, respectively.[23] For FeNC-900, only one peak attached to Fe—N bonding was observed, indicating that the Fe species in FeNC-900 existed as single atoms with Fe—N coordination. Two main peaks affiliated with Fe—N bonding and Fe-Fe bonding were detected in the EXAFS spectra of FeNC-1000 and FeNC-1100, which suggests that the Fe atoms in FeNC-1000 and FeNC-1100 were co-coordinated with the adjacent Fe/N atoms. The XAFS results showed that the thermal migration of Fe atoms during pyrolysis was temperature-controlled, and the coordination structure of Fe species evolved from Fe-N coordination to Fe-N/Fe-Fe co-coordination with increasing temperature, in agreement with HAADF-STEM results. The wavelet transforms of Fe foil and FeNC-900/1000/1100 further confirmed the Fe—N coordination in FeNC-900 and Fe—N/Fe—Fe co-coordination in FeNC-1000/1100 (Figure 2g). The EXAFS fitting results were demonstrated in Figure 2f and Table S3 (Supporting Information), which confirmed the main species in FeNC-900, FeNC-1000 and FeNC-1100 were Fe single atoms with Fe-N_4 coordination, Fe dual atoms with Fe_2N_6 coordination and Fe clusters with Fe-Fe/Fe-N coordination, respectively. The above characterizations together clarified the coordination environments of the Fe species in FeNC-900/1000/1100, which revealed a thermally-controlled evolution of Fe single atoms to Fe dual atoms and Fe clusters during high-temperature pyrolysis.

The controlled modulation of atomic Fe sites provided a simple platform for investigating the ECO_2R processes on single-atom/dual-atom/cluster Fe sites. The ECO_2R performances of FeNC-900/1000/1100 were evaluated in an H-type cell with 0.5 M $KHCO_3$ electrolyte, all tests were performed without *iR* compensation. As we can see from the linear sweep voltammetry curves (LSV) shown in **Figure 3a**, the onset potential of FeNC-1000 for ECO_2R was only ≈150 millivolts (mV) above the theoretical onset potential (−0.11 V vs RHE) for CO_2-to-CO, which was much lower than those of FeNC-900 and FeNC-1100. Notably, NC exhibited little activity for CO_2 reduction, suggesting that the catalytic activities of FeNC-900/1000/1100 for ECO_2R were originated from the atomic Fe sites. In the three atomic Fe catalysts, FeNC-1000 with dual-atom sites showed the most preference for ECO_2R, with maximum polarization current density. These results suggest that the dual-atom Fe sites were more sensitive and active for ECO_2R compared to single-atom and cluster Fe sites.[24] In order to evaluate the catalytic selectivity of these catalysts for ECO_2R, we performed chronoamperometry measurements in the potential range of −0.3 to −0.9 V vs RHE. The gas-phase and liquid-phase products were detected by an online gas chromatography (GC) and an offline ^1H nuclear magnetic resonance (NMR). As shown in Figure S13 (Supporting Information), no liquid product was detected during ECO_2R, and FeNC-1000 achieved FE_{CO} above 92% over a wide potential range from −0.4 V to −0.9 V vs RHE, breaking the selectivity limitation of single-atom sites (FeNC-900) for ECO_2R to CO (maximized FE_{CO} of 66.5% at −0.6 V vs RHE). Besides, FeNC-1100 also exhibited a higher CO selectivity than FeNC-900, which further suggested that the Fe-Fe bonding in atomic Fe sites promoted selective CO_2 reduction to CO (Figure 3b).[13b] Benefitting from the high selectivity and activity toward electrochemical CO production on dual-atom Fe sites, FeNC-1000 attained a maximized j_{CO} of ≈40 mA cm^{-2}, which was 10 times higher than that of FeNC-900 (Figure 3c). The Nyquist plots in Figure S14 (Supporting Information) showed that the anchoring of atomic Fe sites on carbon carriers reduced the charge transfer resistance, which led to an accelerated charge transfer between the Fe sites and the reactants/intermediates during ECO_2R, resulting in the faster reaction kinetics for CO_2 conversion to CO.[25] We also performed electrochemical capacitance measurements (Figure S15, Supporting Information) on NC and various atomic Fe catalysts, in order to obtain the double layer capacitance (C_{dl}) for the evaluation of the electrochemical active surface areas (ECSA).[26] The higher C_{dl} represented a preference for exposing more active sites for electrocatalysis. As shown in Figure 3d, FeNC-1000 exhibited an optimized C_{dl} of 247.34 mF cm^{-2}, superior to that of FeNC-900 (132.86 mF cm^{-2}), FeNC-1100 (58.04 mF cm^{-2}) and NC-1000 (11.65 mF cm^{-2}). These results indicated that FeNC-1000 possessed a maximized exposure of the active sites for ECO_2R. The CO_2 adsorption isotherms in Figure 3e demonstrated that FeNC-1000 had the largest CO_2 adsorption capacity among the four samples, greatly increasing the localized CO_2 concentration near the active Fe sites and thus facilitating the continuous conversion of CO_2-to-CO. Impressively, FeNC-1000 exhibited an excellent stability in long-term electrolysis of CO_2 to CO (Figure 3f), the FE_{CO} remained above 91% even after a 153-h continuous electrolysis at −0.5 V vs RHE, indicating that the dual-atom Fe sites facilitated the desorption of CO products and avoided the CO poisoning. XRD, XPS and HAADF-STEM measurements indicated that the coordination structure and dispersion of Fe species in FeNC-1000 remained stable after long-term electrolysis (Figure S16, Supporting Information). FeNC-1000 also exhibited overwhelming advantages over other published Fe-containing catalysts for ECO_2R in the aspects of potential window width, selectivity, activity and stability.[27] The comparisons of the electrocatalytic performances between FeNC-1000 and recently reported Fe-containing catalysts were shown in Table S4 (Supporting Information).

Above mentioned, we have initially understood that the excellent activity, selectivity and stability of FeNC-1000 originated from the exposed dual-atom sites, excellent electron transfer and high localized CO_2 concentration near the active Fe sites. In order to reveal the key factors influencing the activity/selectivity of CO_2 conversion to CO on different atomic Fe sites, we applied in situ ATR-SEIRAS measurements to monitor the ECO_2R processes on FeNC-900/1000/1100. The schematic diagram of the device was shown in Figure S17 (Supporting Information). As can be seen from the ATR-SEIRAS spectra in Figure 3g, the adsorption peaks located at ≈1250 and ≈1400 cm^{-1} were assigned to the bicarbonate species and C—O stretching in *COOH intermediate, respectively. The peaks at ≈1650 cm^{-1} were assigned to the H—O—H bonding of water, and the peaks at ≈1900 cm^{-1} were attributed to the adsorption of *CO.[28] For FeNC-900/1000/1100, continuous consumption of water during ECO_2R were detected, which represented water dissociations on single-atom/dual-atom/cluster Fe sites. As we all know, the protons from water dissociation had two destinations, to provide hydrogen sources for HER or to participate in CO_2 protonation to form *COOH, the key intermediate in CO_2-to-CO conversion. However, the weak adsorption peaks of *COOH/*CO intermediates in the ATR-SEIRAS spectra of FeNC-900 indicated a preference of HER over ECO_2R on single-atom Fe sites, consistent with the previous

© 2024 Wiley-VCH GmbH

16146840, 2024, 40, Downloaded from https://onlinelibrary.wiley.com/doi/10.1002/aenm.202401364 by Changchun Institution Of, Wiley Online Library on [13/01/2025]. See the Terms and Conditions (https://onlinelibrary.wiley.com/terms-and-conditions) on Wiley Online Library for rules of use; OA articles are governed by the applicable Creative Commons License

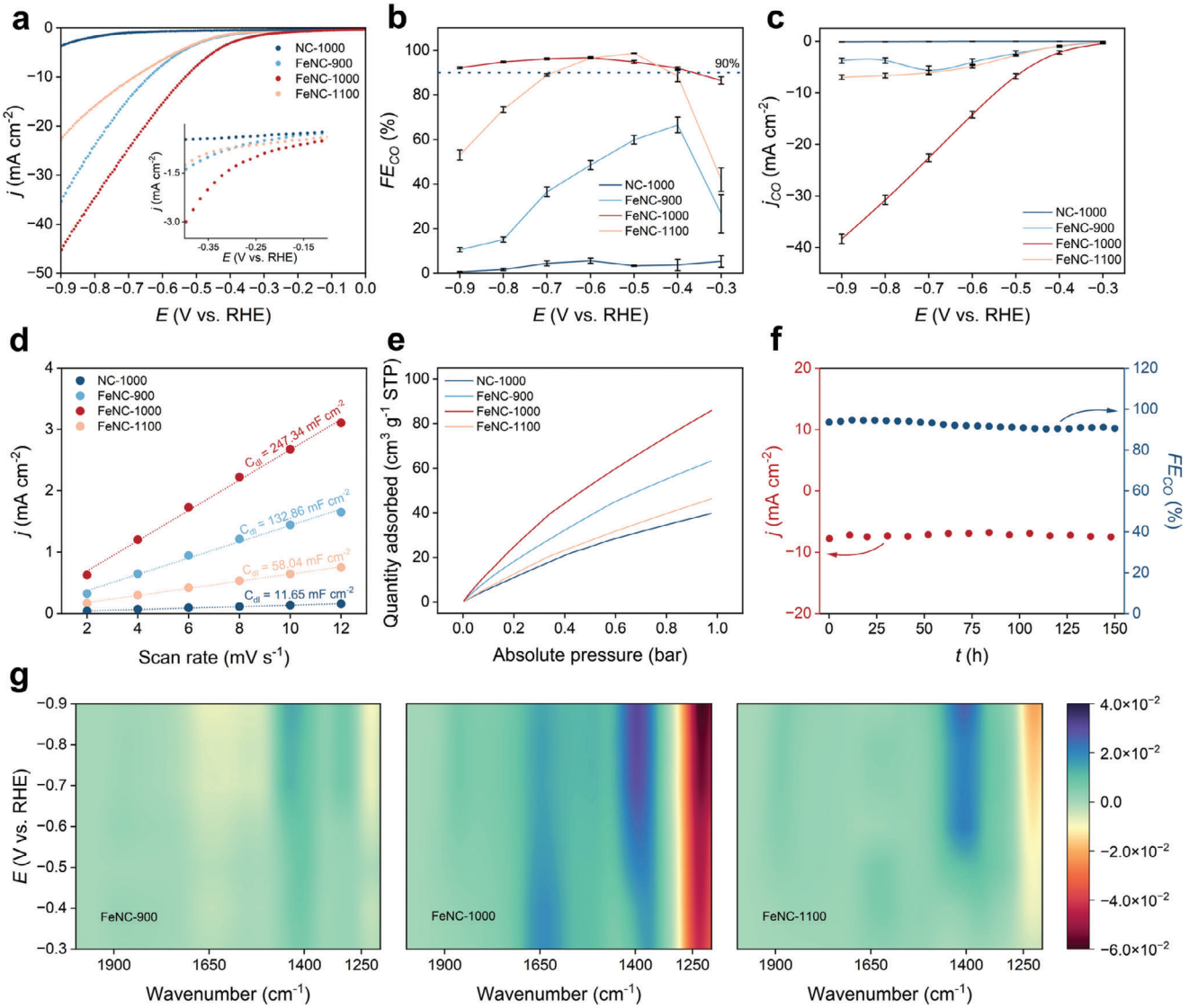

Figure 3. Electrocatalytic CO_2R performance in H-type cell with 0.5 M $KHCO_3$ electrolyte and in situ ATR-SEIRAS measurements. a) LSV curves of NC-1000, FeNC-900, FeNC-1000, and FeNC-1100 in CO_2 saturated electrolytes. b) FEs of CO under different potentials. c) The partial current densities of CO under different potentials. d) C_{dl}s of NC-1000, FeNC-900, FeNC-1000, and FeNC-1100. e) CO_2 adsorption isotherms of NC-1000, FeNC-900, FeNC-1000, and FeNC-1100 at 298 K. f) Long-term stability test of FeNC-1000 in CO_2R under −0.5 V vs RHE. g) In situ ATR-SEIRAS spectra of FeNC-900, FeNC-1000 and FeNC-1100.

electrochemical results. The strong adsorption peaks of water and *COOH intermediates in the ATR-SEIRAS spectra of FeNC-1000 revealed a kinetic equilibrium between water dissociation and CO_2 protonation on dual-atom Fe sites, which benefitted the formation of *COOH intermediate for CO production and suppressed the competing HER. The kinetic isotope effect (KIE) analysis also indicated that the ECO_2R kinetics on FeNC-1000 were dependent on the rate of water dissociation (Figures S18 and S19, Supporting Information).[13a,28a] Although FeNC-1100 exhibited an enhanced CO_2 protonation compared to FeNC-900, the weak adsorption of water on cluster Fe sites limited the proton-feeding for *COOH formation, resulting in the decrease of CO selectivity at high potentials. Overall, the ATR-SEIRAS measurements suggested that regulating the water dissociation on the atomic iron sites for CO_2 protonation was beneficial in promoting the CO_2-to-CO conversion and inhibiting the competitive hydrogen evolution.[5,8,29] The matched kinetics between water dissociation and CO_2 protonation on dual-atom Fe sites endowed FeNC-1000 with optimal selectivity for CO production.

Then we used DFT calculations to elucidate the reaction mechanism of CO_2-to-CO on different atomic Fe sites, the structural models (Figure S20, Supporting Information) were built based on the XAFS results. **Figure 4a** showed the free energies toward ECO_2R to CO on different Fe sites.[30] The Fe_2N_6 site exhibited a weaker adsorption of *CO intermediate compared to FeN_4 and Fe cluster sites, which altered the rate-determining step of CO_2-to-CO from *CO desorption to *CO formation, and prevented

 © 2024 Wiley-VCH GmbH

16146840, 2024, 40, Downloaded from https://onlinelibrary.wiley.com/doi/10.1002/aenm.202401364 by Changchun Institution Of, Wiley Online Library on [13/01/2025]. See the Terms and Conditions (https://onlinelibrary.wiley.com/terms-and-conditions) on Wiley Online Library for rules of use; OA articles are governed by the applicable Creative Commons License

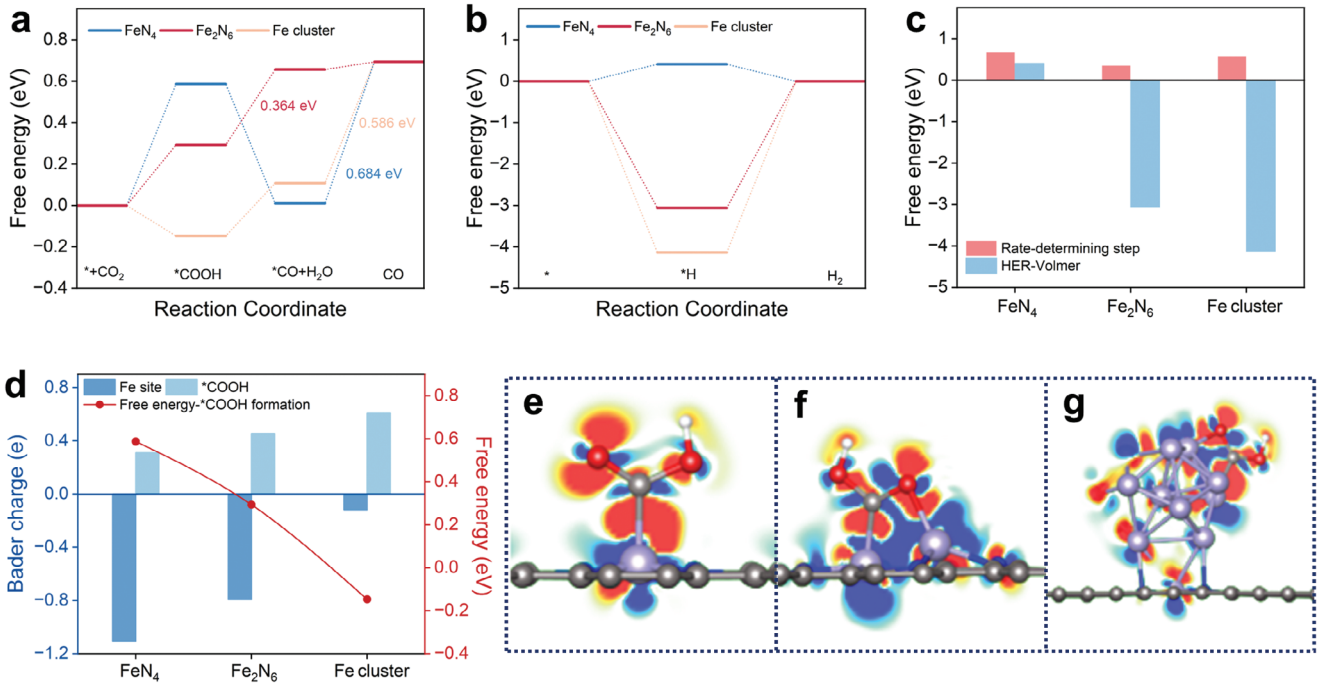

Figure 4. Theoretical calculations. a) Calculated free energy diagram for electrochemical CO_2R to CO on FeN_4 site, Fe_2N_6 site, and Fe cluster site. b) Calculated free energy diagram for HER on FeN_4 site, Fe_2N_6 site, and Fe cluster site. c) Calculated free-energy diagram for rate-determining step of CO_2R and HER on FeN_4 site, Fe_2N_6 site, and Fe cluster site. d) The free energy of *COOH intermediate formation and the charges accumulation/loss of Fe sites and *COOH. Positive and negative values are used to represent charges accumulation and loss, respectively. e–g) Cross-section views of differential charge density maps of *COOH intermediate on e) FeN_4 site, f) Fe_2N_6 site, and g) Fe cluster site. Red and blue represent charge accumulation and loss, respectively.

the poisoning of Fe centers by the adsorbed CO (Figure S21, Supporting Information). Moreover, Fe_2N_6 site exhibited a lower free energy of rate-determining-step for ECO_2R (0.364 eV) compared to that of FeN_4 (0.684 eV) and Fe cluster sites (0.586 eV), suggesting a faster conversion of CO_2 to CO on Fe_2N_6 sites.[31] The free energies of HER-Volmer step on FeN_4, Fe_2N_6, and Fe cluster sites confirm the suppression of competing HER on dual-atom and cluster Fe sites (Figure 4b; Figure S22, Supporting Information). The free energy comparisons of the rate-determining-step for CO_2R and HER-Volmer step on different Fe sites revealed the preference for CO_2R on Fe_2N_6 sites and Fe cluster sites (Figure 4c). The relationship between charge losses from different Fe sites and charge accumulations for *COOH formation demonstrated that the Fe—Fe bonding in atomic Fe sites contributed to the formation of electron-rich centers, which enhanced the adsorption of the key intermediate of *COOH and reduced the free energy for the formation of *COOH (Figure 4d; Figure S23, Supporting Information).[32] The charge differential maps of *COOH on different Fe sites showed better charge transfers between *COOH and Fe_2N_6/Fe cluster sites, further indicating the electron-rich sites promoted the adsorption/activation of *COOH and reduce the free energies for CO production (Figure 4e–g; Figure S24, Supporting Information).[13b] The above DFT calculations revealed that the Fe—Fe bonding in atomic Fe sites promoted the formation of electron-rich centers and regulated the adsorption/activation of the intermediates for CO_2-to-CO conversion. Benefitting from the electron-rich dual-atom Fe sites, FeNC-1000 broke the limited desorption of CO on atomic Fe sites and achieved a faster ECO_2R process.

In view of the excellent catalytic performance of Fe_2N_6 sites for electrochemical CO conversion to CO in H-type cell, we further performed ECO_2R in MEA electrolyzer using FeNC-1000 as catalyst to examine its activity/selectivity for CO production under high current conditions.[33] The pH-universal CO_2 electroreduction performances of FeNC-1000 were evaluated in neutral medium (**Figure 5a–c**), strongly alkaline medium (Figure 5d–f), and strongly acidic medium (Figure 5g–i). In alkaline and neutral mediums, FeNC-1000 exhibited excellent activity and selectivity for ECO_2R reaction. At an average cell voltage (E_{cell}) of 2.02 V in alkaline medium and 2.43 V in neutral medium, FeNC-1000 achieved FE_{CO}s of ≈99% at a current density of 100 mA cm^{-2}.[6,34] In strongly acidic medium, the FE_{CO} still exceeded 96% at a current density of 100 mA cm^{-2} and an average E_{cell} of 2.58 V. Even at an industrial-grade current density of 200 mA cm^{-2}, The FE_{CO} still maintained 86.9%, with a j_{CO} over 170 mA cm^{-2} (pH 2). In the long-term CO_2 conversion to CO at the current density of 100 mA cm^{-2}, FeNC-1000 maintained FE_{CO} of ≈93% after 40-h electrolysis in neutral medium and FE_{CO} of above 97% in a 30-h continuous electrolysis in strongly alkaline medium.[35] Moreover, in strongly acidic medium, FeNC-1000 still maintained the FE_{CO} of ≈90% after a 9-h constant operation. These high activity and selectivity of FeNC-1000 for pH-universal CO_2 electroreduction to CO in MEA electrolyzer suggested that the rationally designed dual-atom Fe catalyst offered a potential application in industrial CO_2 electrolysis.

© 2024 Wiley-VCH GmbH

16146840, 2024, 40, Downloaded from https://onlinelibrary.wiley.com/doi/10.1002/aenm.202401364 by Changchun Institution Of, Wiley Online Library on [13/01/2025]. See the Terms and Conditions (https://onlinelibrary.wiley.com/terms-and-conditions) on Wiley Online Library for rules of use; OA articles are governed by the applicable Creative Commons License

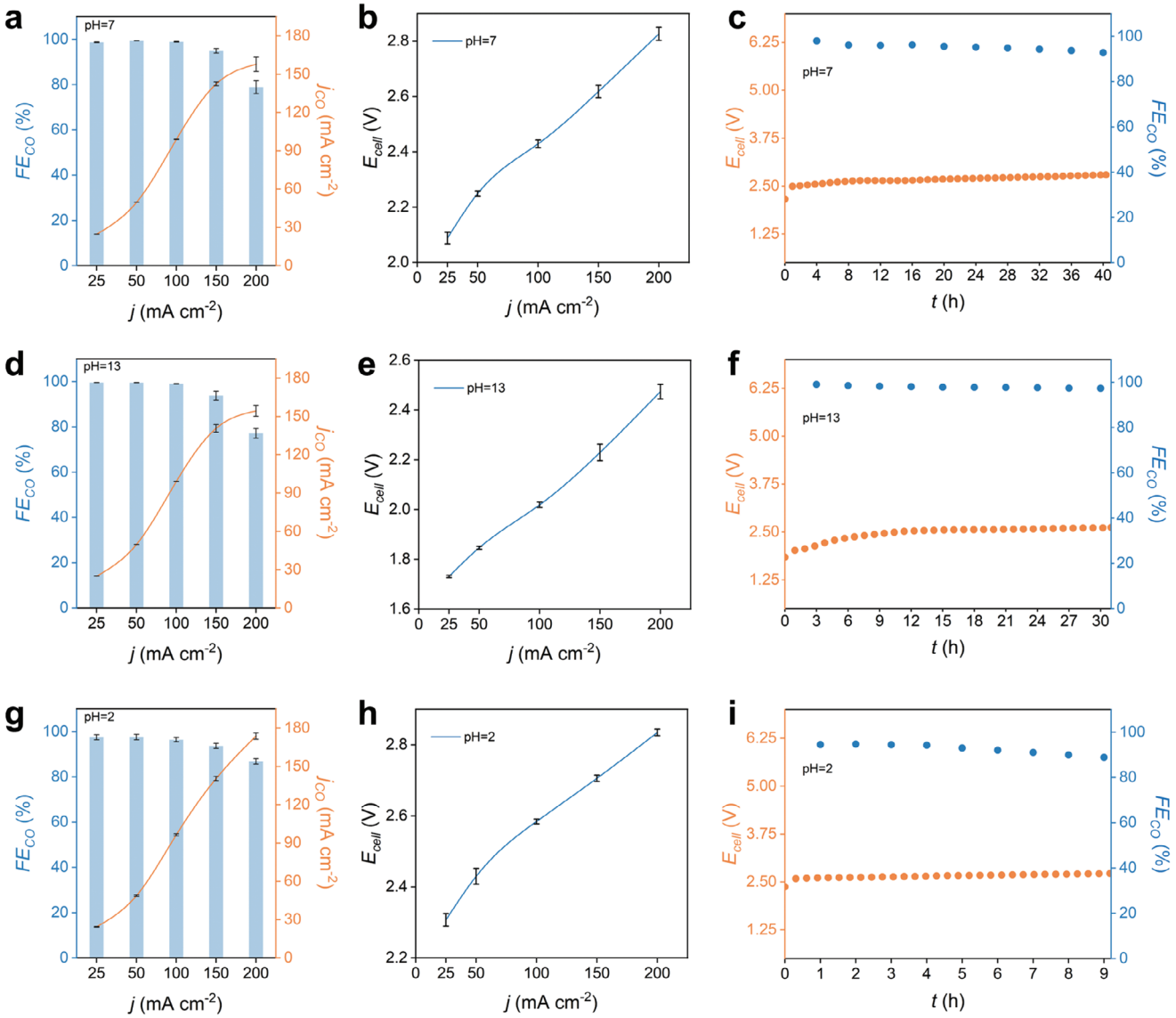

Figure 5. The pH-universal CO_2 electroreduction performance in MEA (0.05 M K_2SO_4, pH 2; 0.1 M $KHCO_3$, pH 7; 0.1 M KOH, pH 13). a) Plots of FE_{CO} and j_{CO} under different current densities. (pH 7) b) Cell voltages under different current densities. (pH 7) c) Long-term stability test of FeNC-1000 in neutral MEA electrolyzer, j = 100 mA cm^{-2}. d) Plots of FE_{CO} and j_{CO} under different current densities. (pH 13) e) Cell voltages under different current densities. (pH 13) f) Long-term stability test of FeNC-1000 in alkaline MEA electrolyzer, j = 100 mA cm^{-2}. g) Plots of FE_{CO} and j_{CO} under different current densities. (pH 2) h) Cell voltages under different current densities. (pH 2) i) Long-term stability test of FeNC-1000 in acidic MEA electrolyzer, j = 100 mA cm^{-2}.

3. Conclusion

In summary, we demonstrated the controllable synthesis of Fe catalysts with different atomic structures by modulating the thermal migration/atomization of Fe species at high temperatures, providing a facile platform for monitoring the ECO_2R processes for efficient CO_2 conversion to CO. The prepared dual-atom Fe catalyst achieved FE_{CO}s above 92% over a wide potential range of −0.4–−0.9 V vs RHE, which broke the selectivity limitation of single-atom Fe sites for ECO_2R to CO. In situ ATR-SEIRAS measurements revealed that the favorable coupling of water dissociation and CO_2 protonation on dual-atom Fe sites promoted the formation of the key intermediate (*COOH) in CO_2-to-CO and suppressed the competing hydrogen evolution. DFT calculations suggested that the Fe-Fe bonding in dual-atom sites induced the formation of electron-rich centers, which optimized the reaction pathway and altered the rate-determining-step for CO production, thus preventing active sites from the poisoning of the adsorbed CO species and accelerating the whole ECO_2R process. Benefitting from the favored kinetics for CO_2-CO conversion on dual-atom Fe sites, FeNC-1000 achieved pH-universal CO_2 electroreduction in alkali-/acid-/bicarbonate-fed MEA electrolyzer, with FE_{CO} exceeded 98% in strongly acidic/alkaline and neutral mediums. This work revealed the significant role of water

© 2024 Wiley-VCH GmbH

16146840, 2024, 40, Downloaded from https://onlinelibrary.wiley.com/doi/10.1002/aenm.202401364 by Changchun Institution Of, Wiley Online Library on [13/01/2025]. See the Terms and Conditions (https://onlinelibrary.wiley.com/terms-and-conditions) on Wiley Online Library for rules of use; OA articles are governed by the applicable Creative Commons License

dissociation on atomic Fe sites toward selective ECO_2R to CO and exhibited a feasible regulation for breaking the desorption limitation of CO products on atomic Fe sites, offering a promising strategy to guide the synthesis of atomic Fe catalysts for achieving industrial-grade CO_2 electrolysis.

Supporting Information

Supporting Information is available from the Wiley Online Library or from the author.

Acknowledgements

This work was supported by the National Natural Science Foundation of China (22171102 and 22090044), the National Key R&D Program of China (2021YFF0500502), the Westlake Education Foundation (Grant No. 103506022001), the Westlake University-Muyuan Joint Research Institute (Grant No. 206006022007), and the Prof. Lu thanks the National Natural Science Foundation of China (Grant No. 92372207). The authors thank the beamline BL14W1 at the Shanghai Synchrotron Radiation Facility.

Conflict of Interest

The authors declare no conflict of interest.

Data Availability Statement

The data that support the findings of this study are available in the supplementary material of this article.

Keywords

CO_2 reduction, diatomic iron sites, pH-universal electrolysis, regulating water dissociation

Received: March 25, 2024
Revised: July 4, 2024
Published online: August 22, 2024

[1] I. Sullivan, A. Goryachev, I. A. Digdaya, X. Li, H. A. Atwater, D. A. Vermaas, C. Xiang, *Nat. Catal.* **2021**, *4*, 952.
[2] S. Jin, Z. Hao, K. Zhang, Z. Yan, J. Chen, *Angew. Chem., Int. Ed.* **2021**, *60*, 20627.
[3] X. She, Y. Wang, H. Xu, S. Chi Edman Tsang, S. Ping Lau, *Angew. Chem., Int. Ed.* **2022**, *61*, 202211396.
[4] M. Wang, Y. Yao, Y. Tian, Y. Yuan, L. Wang, F. Yang, J. Ren, X. Hu, F. Wu, S. Zhang, J. Wu, J. Lu, *Adv. Mater.* **2023**, *35*, 2210658.
[5] S. Chen, X. Li, C.-W. Kao, T. Luo, K. Chen, J. Fu, C. Ma, H. Li, M. Li, T.-S. Chan, M. Liu, *Angew. Chem., Int. Ed.* **2022**, *61*, 202206233.
[6] W. Zhang, S. Liu, Y. Yang, H. Qi, S. Xi, Y. Wei, J. Ding, Z.-J. Wang, Q. Li, B. Liu, Z. Chen, *Angew. Chem., Int. Ed.* **2023**, *62*, 202219241.
[7] Y. Zhou, Q. Zhou, H. Liu, W. Xu, Z. Wang, S. Qiao, H. Ding, D. Chen, J. Zhu, Z. Qi, X. Wu, Q. He, L. Song, *Nat. Commun.* **2023**, *14*, 3776.
[8] L. Zhang, X. Yang, Q. Yuan, Z. Wei, J. Ding, T. Chu, C. Rong, Q. Zhang, Z. Ye, F.-Z. Xuan, Y. Zhai, B. Zhang, X. Yang, *Nat. Commun.* **2023**, *14*, 8311.
[9] S. Li, S. Zhao, X. Lu, M. Ceccato, X.-M. Hu, A. Roldan, J. Catalano, M. Liu, T. Skrydstrup, K. Daasbjerg, *Angew. Chem., Int. Ed.* **2021**, *60*, 22826.
[10] Q. Wang, M. Dai, H. Li, Y.-R. Lu, T.-S. Chan, C. Ma, K. Liu, J. Fu, W. Liao, S. Chen, E. Pensa, Y. Wang, S. Zhang, Y. Sun, E. Cortés, M. Liu, *Adv. Mater.* **2023**, *35*, 2300695.
[11] Q. Wang, K. Liu, J. Fu, C. Cai, H. Li, Y. Long, S. Chen, B. Liu, H. Li, W. Li, X. Qiu, N. Zhang, J. Hu, H. Pan, M. Liu, *Angew. Chem., Int. Ed.* **2021**, *60*, 25241.
[12] a) J. Gu, C.-S. Hsu, L. Bai, H. M. Chen, X. Hu, *Science* **2019**, *364*, 1091; b) H. Lu, J. Tournet, K. Dastafkan, Y. Liu, Y. H. Ng, S. K. Karuturi, C. Zhao, Z. Yin, *Chem. Rev.* **2021**, *121*, 10271.
[13] a) C. Wang, X. Wang, H. Ren, Y. Zhang, X. Zhou, J. Wang, Q. Guan, Y. Liu, W. Li, *Nat. Commun.* **2023**, *14*, 5108; b) X. Zhao, K. Zhao, Y. Liu, Y. Su, S. Chen, H. Yu, X. Quan, *ACS Catal.* **2022**, *12*, 11412; c) K. Li, S. Zhang, X. Zhang, S. Liu, H. Jiang, T. Jiang, C. Shen, Y. Yu, W. Chen, *Nano Lett.* **2022**, *22*, 1557; d) X. Sun, Y. Tuo, C. Ye, C. Chen, Q. Lu, G. Li, P. Jiang, S. Chen, P. Zhu, M. Ma, J. Zhang, J. H. Bitter, D. Wang, Y. Li, *Angew. Chem., Int. Ed.* **2021**, *60*, 23614; e) T. Wang, X. Sang, W. Zheng, B. Yang, S. Yao, C. Lei, Z. Li, Q. He, J. Lu, L. Lei, L. Dai, Y. Hou, *Adv. Mater.* **2020**, *32*, 2002430; f) H. Zhang, J. Li, S. Xi, Y. Du, X. Hai, J. Wang, H. Xu, G. Wu, J. Zhang, J. Lu, J. Wang, *Angew. Chem., Int. Ed.* **2019**, *58*, 14871; g) C. Zhang, S. Yang, J. Wu, M. Liu, S. Yazdi, M. Ren, J. Sha, J. Zhong, K. Nie, A. S. Jalilov, Z. Li, H. Li, B. I. Yakobson, Q. Wu, E. Ringe, H. Xu, P. M. Ajayan, J. M. Tour, *Adv. Energy Mater.* **2018**, *8*, 1703487; h) F. Pan, W. Deng, C. Justiniano, Y. Li, *App. Catal. B Environ.* **2018**, *226*, 463.
[14] a) J. Chen, T. Wang, X. Wang, B. Yang, X. Sang, S. Zheng, S. Yao, Z. Li, Q. Zhang, L. Lei, J. Xu, L. Dai, Y. Hou, *Adv. Funct. Mater.* **2022**, *32*, 2110174; b) Z. W. Seh, J. Kibsgaard, C. F. Dickens, I. Chorkendorff, J. K. Nørskov, T. F. Jaramillo, *Science* **2017**, *355*, eaad4998; c) T. Sun, S. Mitchell, J. Li, P. Lyu, X. Wu, J. Pérez-Ramírez, J. Lu, *Adv. Mater.* **2021**, *33*, 2003075.
[15] a) Q. Hao, Q. Tang, H.-X. Zhong, J.-Z. Wang, D.-X. Liu, X.-B. Zhang, *Sci. Bull.* **2022**, *67*, 1477; b) Q. Hao, H.-x. Zhong, J.-z. Wang, K.-h. Liu, J.-m. Yan, Z.-h. Ren, N. Zhou, X. Zhao, H. Zhang, D.-x. Liu, X. Liu, L.-w. Chen, J. Luo, X.-b. Zhang, *Nat. Synth.* **2022**, *1*, 719.
[16] Y. Zeng, C. Li, B. Li, J. Liang, M. J. Zachman, D. A. Cullen, R. P. Hermann, E. E. Alp, B. Lavina, S. Karakalos, M. Lucero, B. Zhang, M. Wang, Z. Feng, G. Wang, J. Xie, D. J. Myers, J.-P. Dodelet, G. Wu, *Nat. Catal.* **2023**, *6*, 1215.
[17] Y. Wu, L. Ma, J. Wu, M. Song, C. Wang, J. Lu, *Adv. Mater.* **2024**, *36*, 2311698.
[18] a) Y. Wang, J. Hu, T. Ge, F. Chen, Y. Lu, R. Chen, H. Zhang, B. Ye, S. Wang, Y. Zhang, T. Ma, H. Huang, *Adv. Mater.* **2023**, *35*, 2302538; b) Q. Yang, V. A. Kondratenko, A. S. Skrypnik, H. Lund, S. Bartling, J. Weiss, A. Brückner, E. V. Kondratenko, *ACS Catal.* **2023**, *13*, 9064.
[19] a) S. Liu, C. Li, M. J. Zachman, Y. Zeng, H. Yu, B. Li, M. Wang, J. Braaten, J. Liu, H. M. Meyer, M. Lucero, A. J. Kropf, E. E. Alp, Q. Gong, Q. Shi, Z. Feng, H. Xu, G. Wang, D. J. Myers, J. Xie, D. A. Cullen, S. Litster, G. Wu, *Nat. Energy* **2022**, *7*, 652; b) J. Wang, B. Li, Y. Li, X. Fan, F. Zhang, G. Zhang, W. Peng, *Adv. Sci.* **2021**, *8*, 2101824; c) D.-X. Liu, Z. Meng, Y.-F. Zhu, X.-F. Sun, X. Deng, M.-M. Shi, Q. Hao, X. Kang, T.-Y. Dai, H.-X. Zhong, J.-M. Yan, Q. Jiang, *Angew. Chem., Int. Ed.* **2024**, *63*, 202315238.
[20] Y. Wang, B. J. Park, V. K. Paidi, R. Huang, Y. Lee, K.-J. Noh, K.-S. Lee, J. W. Han, *ACS Energy Lett.* **2022**, *7*, 640.
[21] Z. Jin, D. Jiao, Y. Dong, L. Liu, J. Fan, M. Gong, X. Ma, Y. Wang, W. Zhang, L. Zhang, Z. Gen Yu, D. Voiry, W. Zheng, X. Cui, *Angew. Chem., Int. Ed.* **2024**, *63*, 202318246.
[22] a) Y. Zeng, J. Zhao, S. Wang, X. Ren, Y. Tan, Y.-R. Lu, S. Xi, J. Wang, F. Jaouen, X. Li, Y. Huang, T. Zhang, B. Liu, *J. Am. Chem. Soc.* **2023**, *145*, 15600; b) P. Chen, P. Zhang, X. Kang, L. Zheng, G. Mo, R. Wu, J. Tai, B. Han, *J. Am. Chem. Soc.* **2022**, *144*, 14769.
[23] a) A. Mehmood, M. Gong, F. Jaouen, A. Roy, A. Zitolo, A. Khan, M.-T. Sougrati, M. Primbs, A. M. Bonastre, D. Fongalland, G. Drazic, P. Strasser, A. Kucernak, *Nat. Catal.* **2022**, *5*, 311; b) H. Tu, H. Zhang, Y.

 © 2024 Wiley-VCH GmbH

16146840, 2024, 40, Downloaded from https://onlinelibrary.wiley.com/doi/10.1002/aenm.202401364 by Changchun Institution Of, Wiley Online Library on [13/01/2025]. See the Terms and Conditions (https://onlinelibrary.wiley.com/terms-and-conditions) on Wiley Online Library for rules of use; OA articles are governed by the applicable Creative Commons License

Song, P. Liu, Y. Hou, B. Xu, T. Liao, J. Guo, Z. Sun, *Adv. Sci.* **2023**, *10*, 2305194.

[24] a) X. Li, Y. Zeng, C.-W. Tung, Y.-R. Lu, S. Baskaran, S.-F. Hung, S. Wang, C.-Q. Xu, J. Wang, T.-S. Chan, H. M. Chen, J. Jiang, Q. Yu, Y. Huang, J. Li, T. Zhang, B. Liu, *ACS Catal.* **2021**, *11*, 7292; b) J. Tuo, Y. Lin, Y. Zhu, H. Jiang, Y. Li, L. Cheng, R. Pang, J. Shen, L. Song, C. Li, *Appl. Catal. B Environ.* **2020**, *272*, 118960.

[25] P.-Y. Tang, L.-J. Han, F. S. Hegner, P. Paciok, M. Biset-Peiró, H.-C. Du, X.-K. Wei, L. Jin, H.-B. Xie, Q. Shi, T. Andreu, M. Lira-Cantú, M. Heggen, R. E. Dunin-Borkowski, N. López, J. R. Galán-Mascarós, J. R. Morante, J. Arbiol, *Adv. Energy Mater.* **2019**, *9*, 1901836.

[26] X. Yang, X. Li, M. Liu, S. Yang, Q. Xu, G. Zeng, *Angew. Chem., Int. Ed.* **2024**, *63*, 202317785.

[27] a) C. Hu, S. Bai, L. Gao, S. Liang, J. Yang, S.-D. Cheng, S.-B. Mi, J. Qiu, *ACS Catal.* **2019**, *9*, 11579; b) J. Zhang, H. Yang, B. Liu, *Adv. Energy Mater.* **2021**, *11*, 2002473; c) F. Pan, B. Li, E. Sarnello, Y. Fei, X. Feng, Y. Gang, X. Xiang, L. Fang, T. Li, Y. H. Hu, G. Wang, Y. Li, *ACS Catal.* **2020**, *10*, 10803; d) F. Pan, H. Zhang, K. Liu, D. Cullen, K. More, M. Wang, Z. Feng, G. Wang, G. Wu, Y. Li, *ACS Catal.* **2018**, *8*, 3116; e) T. N. Huan, N. Ranjbar, G. Rousse, M. Sougrati, A. Zitolo, V. Mougel, F. Jaouen, M. Fontecave, *ACS Catal.* **2017**, *7*, 1520.

[28] a) W. Ma, S. Xie, T. Liu, Q. Fan, J. Ye, F. Sun, Z. Jiang, Q. Zhang, J. Cheng, Y. Wang, *Nat. Catal.* **2020**, *3*, 478; b) L. Zhang, J. Feng, S. Liu, X. Tan, L. Wu, S. Jia, L. Xu, X. Ma, X. Song, J. Ma, X. Sun, B. Han, *Adv. Mater.* **2023**, *35*, 2209590; c) P.-P. Yang, X.-L. Zhang, P. Liu, D. J. Kelly, Z.-Z. Niu, Y. Kong, L. Shi, Y.-R. Zheng, M.-H. Fan, H.-J. Wang, M.-R. Gao, *J. Am. Chem. Soc.* **2023**, *145*, 8714; d) J. Zhao, P. Zhang, T. Yuan, D. Cheng, S. Zhen, H. Gao, T. Wang, Z.-J. Zhao, J. Gong, *J. Am. Chem. Soc.* **2023**, *145*, 6622.

[29] X. Wang, S. Feng, W. Lu, Y. Zhao, S. Zheng, W. Zheng, X. Sang, L. Zheng, Y. Xie, Z. Li, B. Yang, L. Lei, S. Wang, Y. Hou, *Adv. Funct. Mater.* **2021**, *31*, 2104243.

[30] E. Skúlason, T. Bligaard, S. Gudmundsdóttir, F. Studt, J. Rossmeisl, F. Abild-Pedersen, T. Vegge, H. Jónsson, J. K. Nørskov, *Phys. Chem. Chem. Phys.* **2012**, *14*, 1235.

[31] J. Wang, Y. Song, C. Chen, X. Zhao, W. Fan, *ACS Catal.* **2023**, *13*, 15794.

[32] J. Yin, J. Jin, Z. Yin, L. Zhu, X. Du, Y. Peng, P. Xi, C.-H. Yan, S. Sun, *Nat. Commun.* **2023**, *14*, 1724.

[33] a) H. Yun, W. Choi, D. Shin, H.-S. Oh, Y. J. Hwang, *ACS Catal.* **2023**, *13*, 9302; b) G. Deng, H. Yun, M. S. Bootharaju, F. Sun, K. Lee, X. Liu, S. Yoo, Q. Tang, Y. J. Hwang, T. Hyeon, *J. Am. Chem. Soc.* **2023**, *145*, 27407; c) S. Yan, Z. Chen, Y. Chen, C. Peng, X. Ma, X. Lv, Z. Qiu, Y. Yang, Y. Yang, M. Kuang, X. Xu, G. Zheng, *J. Am. Chem. Soc.* **2023**, *145*, 26374; d) L. Ge, H. Rabiee, M. Li, S. Subramanian, Y. Zheng, J. H. Lee, T. Burdyny, H. Wang, *Chem* **2022**, *8*, 663.

[34] W. Li, Z. Yin, Z. Gao, G. Wang, Z. Li, F. Wei, X. Wei, H. Peng, X. Hu, L. Xiao, J. Lu, L. Zhuang, *Nat. Energy* **2022**, *7*, 835.

[35] a) H.-G. Qin, Y.-F. Du, Y.-Y. Bai, F.-Z. Li, X. Yue, H. Wang, J.-Z. Peng, J. Gu, *Nat. Commun.* **2023**, *14*, 5640; b) Q. Hao, D.-X. Liu, H.-X. Zhong, Q. Tang, J.-M. Yan, *Chem. Catal.* **2023**, *3*, 100542.

 © 2024 Wiley-VCH GmbH

16146840, 2024, 40, Downloaded from https://onlinelibrary.wiley.com/doi/10.1002/aenm.202401364 by Changchun Institution Of, Wiley Online Library on [13/01/2025]. See the Terms and Conditions (https://onlinelibrary.wiley.com/terms-and-conditions) on Wiley Online Library for rules of use; OA articles are governed by the applicable Creative Commons License